

Mathematical Simulation of Glioblastoma
Multiform Under Treatment

by

Austin L Trent

A Thesis Presented in Partial Fulfillment
of the Requirements for the Degree
Master of Arts

Approved April 2020 by the
Graduate Supervisory Committee:

Eric Kostelich, Chair
Abba Gumel
Yang Kuang

ARIZONA STATE UNIVERSITY

May 2020

ABSTRACT

The analysis focuses on a two-population, three-dimensional model that attempts to accurately model the growth and diffusion of glioblastoma multiforme (GBM), a highly invasive brain cancer, throughout the brain. Analysis into the sensitivity of the model to changes in the diffusion, growth, and death parameters was performed, in order to find a set of parameter values that accurately model observed tumor growth for a given patient. Additional changes were made to the diffusion parameters to account for the arrangement of nerve tracts in the brain, resulting in varying rates of diffusion. In general, small changes in the growth rates had a large impact on the outcome of the simulations, and for each patient there exists a set of parameters that allow the model to simulate a tumor that matches observed tumor growth in the patient over a period of two or three months. Furthermore, these results are more accurate with anisotropic diffusion, rather than isotropic diffusion. However, these parameters lead to inaccurate results for patients with tumors that undergo no observable growth over the given time interval. While it is possible to simulate long-term tumor growth, the simulation requires multiple comparisons to available MRI scans in order to find a set of parameters that provide an accurate prognosis.

ACKNOWLEDGEMENTS

The work detailed in the paper is supported by a grant from the Arizona Biomedical Research Commission. The author would like to thank Dr. Mark Preul and Dr. Chad Quarles from the Barrow Neurological Institute for providing MR images and informative discussions, as well as Dr. Steffen Eikenberry and Lifeng Han for informative discussions.

TABLE OF CONTENTS

	Page
LIST OF TABLES	iv
LIST OF FIGURES	v
INTRODUCTION	1
MODEL AND METHOD	7
Model	7
Method	10
Preprocessing	11
Isotropic Versus Anisotropic Diffusion	12
Implementation	13
Finding the Best-fit Parameters	14
RESULTS	17
Parameter Sensitivity Analysis	17
Best Fit Parameters	19
With Edema	19
Without Edema	19
Visual Results	21
Long-term Analysis	22
DISCUSSION	42
CONCLUSION	45
BIBLIOGRAPHY	46
APPENDIX	48
I FINITE DIFFERENCE IMPLEMENTATION	48
II NUMERICAL METHOD	51

LIST OF TABLES

Table		Page
1	Initial Parameters	13
2	Maximum Isotropic Rate of Change For ρ_1 , ρ_2 , And D	17
3	Maximum Isotropic Rate of Change For k_1 , k_2 , And k_3	18
4	Maximum Anisotropic Rate of Change For ρ_1 , ρ_2 , And D	18
5	Maximum Anisotropic Rate of Change For k_1 , k_2 , And k_3	19
6	Best-fit Parameters for Isotropic Simulations, With Edema	20
7	Best-fit Parameters for Anisotropic Simulations, With Edema	20
8	Best-fit Parameters for Isotropic Simulations, Without Edema	21
9	Best-fit Parameters for Anisotropic Simulations, Without Edema	22

LIST OF FIGURES

Figure		Page
1	Patient 011 Best-fit With Edema	23
2	Patient 018 Best-fit With Edema	24
3	Patient 026 Best-fit With Edema	25
4	Patient 028 Best-fit With Edema	26
5	Patient 029 Best-fit With Edema	27
6	Patient 030 Best-fit With Edema	28
7	Patient 036 Best-fit With Edema	29
8	Patient 039 Best-fit With Edema	30
9	Patient 045 Best-fit With Edema	31
10	Patient 011 Best-fit Without Edema	32
11	Patient 026 Best-fit Without Edema	33
12	Patient 029 Best-fit Without Edema	34
13	Patient 036 Best-fit Without Edema	35
14	Patient 045 Best-fit Without Edema	36
15	Patient 011 Long-term	37
16	Patient 026 Long-term	38
17	Patient 028 Long-term	38
18	Patient 029 Long-term	39
19	Patient 036 Long-term	40
20	Patient 045 Long-term	41
21	Anisotropic Best-fit Scatter Plot	43
22	Isotropic Best-fit Scatter Plot	43

1. Introduction

Glioblastoma multiforme (GBM), one of the most aggressive types of brain cancer, is often fatal and difficult to treat, with most patients surviving for less than two years after diagnosis (Stupp 2005). Current therapy consists of a thorough surgical resection followed by radiotherapy, along with adjuvant temozolomide or carmustine (Stupp 2005). While therapy can extend the survival time of a patient, GBM is resistant to medical treatments such as chemotherapy or surgical resections for a number of reasons. Because of the highly diffusive nature of GBM, surgical resections are ineffective even though they may relieve pressure-induced symptoms. Resections are particularly ineffective in highly diffusive tumors, where a total resection may remove as little as 12 percent of the total cancer population (Murray 2003). Furthermore, GBM tumors regularly reappear at the boundary of the resection even when brain tissue beyond the rim of the visible tumor is excised (Han 2019). While a total resection may offer some survival benefit, surgery may only increase a patient's survival by about two months (Han 2019, Murray 2003). Chemical treatments, such as chemotherapy, are similarly ineffective for other reasons. In addition to the difficulties provided by the blood-brain barrier, the heterogeneity of the tumors provides a natural drug resistance that must be accounted for in order to effectively treat all types of cancer cell present. Furthermore, it has been observed that cancer cells outside the main tumor do not appear to undergo mitosis, limiting the effectiveness of radiation therapy and other "cell-cycle-dependent" treatments (Murray 2003). Other treatments, such as oral steroids, may be prescribed to treat neurological issues resulting from edema, but analysis infers that steroids are not associated with an increase in survival time (Petrelli 2020). However, survival times can be extended by an average of 2.5 months if patients who undergo chemotherapy are also prescribed temozolomide, with a two-year survival rate of 26.5% for patients receiving temozolomide and radiotherapy as opposed to 10.4% with just radiotherapy (Stupp 2005). As a result of these difficulties, long-term survival for a patient is

rare, even with early detection and treatment.

Like other gliomas, GBM diffuses throughout the brain in a highly invasive manner. While there can be significant variance with regard to tumor growth and diffusion rates, rat experiments show that glioma cells can appear throughout the central nervous system within seven days (Murray 2003, Rutter 2017). In humans, while a majority of the tumor cells are located in the tumor core, the surrounding enhancing rim is capable of rapid growth, and lower numbers of tumor cells are capable of diffusing even further beyond the enhancing rim. As an example, if the area of a detectable tumor on the edge of the brain possesses a diameter of 3cm, there may potentially be cancer cells that have diffused as far as the corpus callosum (Murray 2003). Even with the use of MRI imaging, the density of the cancer cell population and the rate of diffusion beyond the tumor can only be estimated, with some works hypothesizing that only 94 percent of the total cancer population is observable in T1 and T2 MRIs (Swanson 2008).

The highly lethal nature of GBM cancer, as well as the ineffectiveness of these treatments, have inspired a number of mathematical models which aim to provide accurate tumor growth and diffusion dynamics. Variants on the Fisher-Kolmogorov equation (initially proposed as a model for genetic drift in a population) were first suggested as models for GBM growth by J. D. Murray, with the original Fisher-Kolmogorov model given by the following (Fisher 1937):

$$\frac{\partial c}{\partial t} = \nabla \cdot (D \nabla c) + \rho c \left(1 - \frac{c}{K}\right), \quad (1)$$

where D represents the rate of diffusion, $c(x, t)$ represents the tumor population at time t and location x , ρ represents the growth rate, and K represents the carrying capacity. The Fisher-Kolmogorov model (and variations on it) are capable of accurately representing the diffusivity of GBM, as well as recurrence near the resection as typically observed in patient

MRIs (Murray 2003). Furthermore, the model produces a traveling-wave solution with velocity $2\sqrt{D\rho}$, which matches the observed linear increase in the radius of an observable tumor over time. Given that the traveling-wave speed details how fast the cancer progresses, the growth and diffusion parameters have a large impact on the survival time of the patient, and can be approximated by comparing available patient MRIs (Murray 2003). Thus, an accurate estimation of ρ and D for a given patient is necessary in order to model tumor growth over time.

Other works that have made use of the Fisher-Kolmogorov model aimed to estimate the survival time of a patient depending on ρ , D , and the extent of surgical resection, and found that the velocity of tumor growth (as defined above) can accurately predict survival time in a patient, with the ratio having a nonlinear effect on the associated T1 and T2 radii. Calculations of the ratio D/ρ varied over a wide range, but there was no significant variation between patients that had been prescribed steroids and patients that had not had steroids. Similarly, they found no significant variation in the ratio D/ρ between patients with no resections, partial resections, or full resections (Swanson 2008).

Earlier analyses were based on a variety of ‘virtual treatments’ included no/partial resections (grouped together due to similar survival times), full resections, and resections 125% past the observable tumor’s radii, with the survival times of these virtual treatments compared with the patient’s actual survival time. Survival time for the virtual cases was calculated by finding the time required for the tumor to grow to a radius of 3cm (Swanson 2008). While some other works estimate survival time based on an average lethal tumor radius of 3cm, the actual lethal radius for a given patient can fall within a large range, and many other works have found no relation between tumor size and survival time (Murray 2003, Swanson 2008). The comparison found that, for their sample of patients, survival times were longer for patients with total resections as opposed to partial/no resections. However, comparisons with the virtual data suggest the increased survival times for patients with to-

tal resections is partially accounted for by the fact that some of the total resection patients had smaller tumors to begin with, and total resections may provide an increase in survival time of only 17.1 weeks, suggesting that the 'better' patients are typically chosen for total resections. However, the analysis in question relied on pre-op MRI scans with no second set of MRIs available. The paper notes that a second set of MRIs would allow the analysis to rely on exact values, rather than estimations, of the individual values ρ and D .

Other authors have built on model 1 by including the effect of radiation therapy in order to model tumor growth under treatment (Rockne 2008). To account for the effect of radiation therapy on cancer cell populations, Rockne et al. (2008) produced the following model:

$$\frac{\partial c}{\partial t} = \nabla \cdot (D(x)\nabla c) + \rho c - R(x, t)c \quad (2)$$

Here, $R(x, t)$ represents the effect of radiation therapy at time t and location x . While model 2 suggests that $D(x)$ may vary spatially, the analysis focuses only on the isotropic case, where the rate of diffusion remains constant in all directions. As a result, there is no preferred direction of travel, with diffusion mainly dictated by Brownian motion. Analysis was performed on virtual tumors, which were allowed to grow to 10-20mm in size before radiation therapy was included, then for an additional 100 days afterwards. While the parameters $D = 1.43 \text{ cm}^2/\text{year}$ and $\rho = 16.25/\text{year}$ remained constant between simulations, treatment schedules and dose distributions varied between simulations. While the analysis found that radiation treatments on a daily basis (the conventional treatment) are much more effective than treatments given several times per day, it is unknown if these results remain true for various values of D and ρ . Additionally, analysis was not performed on a virtual tumor following a resection.

While previous works have approximated tumor growth rates and survival times relatively accurately, there are some factors that have not been considered (Murray 2012, Swanson 2008). For example, the Fisher-Kolmogorov equation does not include a death term to account for radiation therapy or other treatments and while later works may analyze a model with such a death term, they do not necessarily consider the toxicity or space-limiting effects of necrotic cells on the growth/diffusion of cancer cells (Rockne 2008). Necrosis is a defining feature of GBM, particularly for tumors with high growth and low diffusion parameters. Thus, an inclusion of a death term that replicates necrosis could capture an important aspect of GBM growth without overly complicating the model (Murray 2003). Additionally, most works do not analyze the growth of GBM under treatment, and while some works make note of the impact of the brain's geometry on the rate of diffusion, or allow D to vary depending on whether diffusion occurs in white or gray matter, only isotropic diffusion is considered, with the additional assumption that tumor expansion is symmetric (Han 2019, Murray 2003, Rockne 2008). In reality, the rate of diffusion is highly directionalized. Since the brain is made up of nerve tracts, it is likely that, for a given voxel, cancer cells in the region will move along the nerve tracts, rather than across them. To account for the varying arrangement of the nerve tracts, the diffusion rate would need to vary with respect to the direction of diffusion. Given the fact that some models have shown the wavespeed $2\sqrt{D\rho}$ dictates survival time, while others have shown the rate of diffusion to be more important than the rate of proliferation or necrosis in determining survival time, it seems prudent to consider a model with anisotropic diffusion to capture these characteristics of the brain (Mahan 2013, Murray 2003, Swanson 2008). Furthermore, previous works typically did not have access to a series of MRIs, requiring estimates of parameters that could be measured directly by comparing a patient's MRIs (Swanson 2008). While a simple model that accurately approximates the data is ideal, the inclusion of anisotropic diffusion and a death term that accounts for necrosis and quiescence may be

more accurate than previous models while remaining relatively simple, and such a model would be even more accurate if several patient MRIs were available to directly measure the patient's parameters.

The next section details the model used for our analysis, as well as the method used to estimate the growth and diffusion parameters for several patients. For a given set of best-guess parameters, we include the results of the simulation for both short and long intervals of time. These results are directly compared with the patient's MRI scans (if available) in order to determine the model's ability to mimic the patient's observed tumor growth with our chosen set of parameters.

2. Model and Method

The following model was chosen for analysis because it accounts for cancer cell quiescence and the fact that living cancer cells are inhibited by the presence of quiescent cells, due to a limited amount of space. Furthermore, the model can be used for patients who are undergoing treatment, and previous analysis of the model has shown that the parameters can be estimated analytically from one or two patient MRIs (Han 2019).

2.1 Model

Our model for the growth of GBM cancer is governed by the following reaction-diffusion equations:

$$\frac{\partial p}{\partial t} = \nabla \cdot \left[\left(\frac{D(x)p}{p+q} \right) \nabla(p+q) \right] + \tilde{g}(w)p - \tilde{\delta}(w)p \quad (3)$$

$$\frac{\partial q}{\partial t} = \nabla \cdot \left[\left(\frac{D(x)q}{p+q} \right) \nabla(p+q) \right] + \tilde{\delta}(w)p \quad (4)$$

with

$$w = 1 - p - q.$$

The model supposes there are two types of cancer cells: proliferative cells and quiescent cells, with cell densities at time t and location x given by $p(x, t)$ and $q(x, t)$, respectively. Here, $\tilde{g}(w)p$ represents the growth rate of the proliferative cells, while $\tilde{\delta}(w)p$ represents the quiescent rate. For the purposes of this model, necrotic cells are considered quiescent cells, even though not all quiescent cells are considered necrotic (Han 2019). As proliferative cells become quiescent cells (but not vice versa), the growth rate for the quiescent cells is equal to the quiescent rate for the proliferative cells, with no corresponding death rate. The birth and quiescent rates are both dependent on the variable w , which represents the availability of some limiting quantity (such as space or nutrients) and is hereafter referred to as the growth factor. Since $p+q$ takes values between 0 and 1, so does the growth factor w . Additionally, the constraints on $p+q$ allow the model to account for limited proliferative

cell growth due to the presence of quiescent cells. Furthermore, we note $\tilde{g}(w) = \rho g(w)$, where ρ represents the growth rate with maximum growth factor and $g(w) = B(w; \alpha_g, \beta_g)$. Here, $B(w; \alpha, \beta)$ represents the beta cumulative density function with shape parameters α and β . In our case, $\alpha_g = 1$ and $\beta_g = 3$. Similarly, we have $\tilde{\delta}(w) = k\delta(w)$, with k representing the death rate with no growth factor and $\delta(w) = 1 - B(w; \alpha_\delta, \beta_\delta)$. In our case, we have $\alpha_\delta = 2$, $\beta_\delta = 2$. The shape parameters $\alpha_g = 1$, $\beta_g = 3$, $\alpha_\delta = 2$, and $\beta_\delta = 2$ allow for an analytical estimation of ρ , k , and D , but there are other choices for the shape parameter values that still allow for identifiable parameters (Han 2019).

The following constraints are placed on $g(w)$ and $\delta(w)$ to make the model biologically reasonable:

$$\tilde{g}'(w) \geq 0, \quad \tilde{\delta}'(w) \leq 0, \quad \tilde{g}(1) \geq \tilde{\delta}(1) = 0, \quad \tilde{\delta} \geq \tilde{g}(0) = 0. \quad (5)$$

The constraints on the growth and quiescence functions implies that the rate of growth decreases with decreasing growth factor while the rate of quiescence increases. The constraints in 5 allow us to ensure $0 \leq p + q \leq 1$ for all t . Furthermore, the constraints account for the growth rate slowing in the presence of quiescent cells due to a lack of space (Han 2019).

The diffusion terms in Equations 3 and 4 are best described as *cross diffusion* terms, where the concentration of one cancer cell population can cause a flux in the other population (Han 2019). Furthermore, these diffusive terms assume there is no change in D with respect to the direction of diffusion. A variant of the model, which does not assume the diffusion is isotropic, is considered later in the text.

Han's analysis of the model attempted to use a traveling-wave solution to approximate the growth and diffusion of a tumor by considering the model in one spatial dimension:

$$\frac{\partial p}{\partial t} = \frac{\partial}{\partial x} \left[\left(\frac{Dp}{p+q} \right) \frac{\partial}{\partial x} (p+q) \right] + \rho g(w)p - k\delta(w)p \quad (6)$$

$$\frac{\partial q}{\partial t} = \frac{\partial}{\partial x} \left[\left(\frac{Dq}{p+q} \right) \frac{\partial}{\partial x} (p+q) \right] + \rho g(w)p - k\delta(w)p \quad (7)$$

Han (2019) concluded that the asymptotic speed of the traveling wave solution matches the minimum speed with $c = c_{\min} = 2\sqrt{\hat{\rho}}$, with $\hat{\rho} = \rho/k$. To approximate the parameters of the model from a set of given MRI data, three radii were derived: R_0 , R_1 , and R_2 , representing (respectively) the radius of the inner necrotic core, the radius to the edge of the enhancing rim, and the radius to the edge of the edema. These are used to calculate $L_1 = R_1 - R_0$ and $L_2 = R_2 - R_1$.

For a patient with two sets of pre-treatment MRI scans available for comparison, parameters are estimated by calculating

$$L_1 = \frac{2\sqrt{D\rho}}{k} \int_{w_1^-}^{w_1^+} \frac{dz}{dw} dw, \quad (8)$$

$$L_2 = \frac{2\sqrt{D\rho}}{k} \int_{w_2}^{w_1^-} \frac{dz}{dw} dw, \quad (9)$$

$$f(\hat{\rho}) = \frac{L_1}{L_2}. \quad (10)$$

From L_1 , L_2 , and $f(\hat{\rho})$, $\hat{\rho}$ can be computed analytically, which is then used to find the remaining parameters.

If only a single set of MRI images are available, parameters were estimated by supposing that, for $0 \leq t \leq t^*$, quiescence is negligible and proliferative cells grow exponentially, and for $t > t^*$, the tumor grows as a traveling wave with speed $2\sqrt{\rho D}$. If

$$R_i = t^* \sqrt{4D\rho - \frac{4D}{t^*} \ln \left(\frac{a_i(4\pi D t^*)^{3/2}}{p_0} \right)} \quad (11)$$

and R_1 and R_2 are the radii at $t = t^*$, then

$$\frac{R_1 - R_1^*}{2\sqrt{\rho D}} = \frac{R_2 - R_2^*}{2\sqrt{\rho D}}. \quad (12)$$

Together with Equations 8 and 9, $\hat{\rho}$ can be estimated (Han 2019).

The results of Han's analytical analysis (2019) suggest that parameters can generally be accurately estimated, but L_2 may be inaccurate for small values of $\hat{\rho}$, likely due to the assumption that $c = 2\sqrt{\hat{\rho}}$ is large. Furthermore, there is considerable variation among the estimated parameters between patients, with values of D ranging from 0.0687 to 1.2791, values of ρ ranging from 0.1652 to 0.2624, and values of k ranging from 0.0106 to 0.7819, which matches the observations of other works, some of which observed up to a 10-fold variation in the growth and diffusion parameters (Murray 2003, Rockne 2008, Swanson 2008). The diffusion coefficient plays a large role, both in the linearized wave head and the characteristic length (where its square root scales the space), while the scale-invariant part of the wave profile is determined by the form of the birth and death functions. Lastly, previous analysis of the model suggests that there is likely some variation in these parameters over time, requiring frequent reference to available MRI sets in order to provide accurate tumor growth.

2.2 Method

Our analysis focuses on six parameters that relate to the growth rate ρ , the quiescent rate k , and the diffusion rate in different regions of the brain. Two of these parameters are related to the growth rate ρ : ρ_1 refers to the growth rate in the white matter and edematous regions of the brain, while ρ_2 refers to the growth rate in the gray matter regions, as well as the enhancing rim and the tumor core. The other three parameters relate to the quiescent rate k : k_1 corresponds to the rate of quiescence in the white matter, gray matter, and edematous regions of the brain, while k_2 and k_3 correspond to the quiescent rate in

the enhancing rim and the tumor core, respectively. The sixth parameter, D , determines the rate of diffusion everywhere in the brain. In doing so, we make two assumptions: the rate of diffusion is ten times as high for proliferative cells in comparison to quiescent cells regardless of where diffusion takes place, and the rate of diffusion is twice as high in white matter as it is anywhere else for both cell types. More specifically, we let the value of D correspond to the rate of diffusion in white matter for the quiescent cells, then calculate the rate of diffusion for quiescent cells in regions other than white matter as $D/2$, the rate of diffusion in white matter for proliferative cells as $10D$, and the rate of diffusion for proliferative cells in regions other than white matter as $5D$ (Murray 2003). Simulations are run with appropriate values for the given parameters.

2.2.1 Preprocessing

The analysis focuses on ten patients whose MRIs have been provided by the Barrow Neurological Institute. Previous analysis of some of these patients in 2D indicated a model of this type has the capability to predict future tumor growth (Eikenberry 2009). To prepare the simulations, the patients' MRI scans have been fit to a standardized brain space via the MATLAB software package Statistical Parametric Mapping 12, with the use of the default standard brain (SPM 2020). For reference, the MRI scans and the standardized brain are split into voxels that are 1mm^3 in size. While mapping every patient to the same brainspace allows for easier comparisons between MRI scans and between patients, there is naturally some error that occurs when warping a patient MRI to a standardized brain space. The warping error is more pronounced in patients with tumors large enough to cause mass effect within the brain. However, while this may be visually noticeable in some patients, it is hard to quantify how much error to expect when mapping patients to a standard brainspace.

Afterwards, segmentations of the two comparison MRIs are created manually in Slicer 3D (Kikinis 2014). For a given patient, segmentations are created for the tumor core, the enhancing rim, the edema, and (if necessary) the resection. Tumor core, enhancing rim,

and resection segmentations are created using T2 scans, while the edema is created with a T1 scan. In some cases, T2 MRI scans are not available for a given day. In such cases, the edema can not be accurately approximated, and is thus left out of the error calculations. The segmentations of the first set of MRIs are used to initialize the simulation on a per voxel basis. Each voxel in the simulation can be labelled as belonging to the tumor core, the enhancing rim, or the edema, with initial proliferative tumor cell populations of 0.99, 0.5, and 0.01, respectively. Alternatively, voxels in the region indicated by the resection segmentation are relabelled as CSF, preventing any growth, with the end result being an imposed cell population of 0 in the region (Swanson 2008). Unlabelled voxels are assumed to have no tumor cell population at the start of the simulation. The segmentations of the second set of MRIs are used for error calculations, as detailed later in the results section.

2.2.2 Isotropic Versus Anisotropic Diffusion

Two variants of the code are used to perform these simulations with either isotropic or anisotropic diffusion. To accurately model the anisotropic diffusion needed, a variant on the original isotropic diffusion code references a set of diffusion tensor values to adjust the rate of diffusion in any given direction. To create a gradient vector that is an appropriate size for the corresponding diffusion tensor, a 27-point stencil is used to calculate derivatives in the x , y , and z directions, although not all points are used to calculate these derivatives. The anisotropic diffusion code differs from the isotropic diffusion code, which uses all points in the 27-point stencil to calculate derivatives in the x , xy , xz , y , yz , z , and xyz directions. While the use of a 27-point stencil may be computationally expensive, the increased accuracy allows for a timestep that $8/3$ times larger than with a 7-point stencil. Both the isotropic and anisotropic code calculated the diffusion term with the use of a finite difference method, as described in Appendix I.

For the anisotropic code, diffusion tensor data from DTI-TK was used to calculate the diffusion term (Zhang 2018). As with the patient MRIs, the diffusion tensor data was

Table 1. The initial parameter values for the isotropic and anisotropic simulations, for all patients.

Version	ρ_1	ρ_2	k_1	k_2	k_3	D
Isotropic	0.04	0.02	0.01	0.02	0.04	0.04
Anisotropic	0.04	0.02	0.01	0.02	0.04	4.00

mapped to a standardized brain space via SPM12 (“SPM - Statistical Parametric Mapping”). Afterwards, negative values in the diffusion tensor data were set to 0, to ensure all diffusion tensors remained positive definite. Analysis of the eigenvalues of these diffusion tensors suggests they are indeed positive definite, with a maximum eigenvalue of 0.00329.

2.2.3 Implementation

The simulations were implemented in Fortran. Given the existence of the growth and quiescence terms, the PDE equations that define the model as defined in Equations 3 and 4 are fairly stiff and require the use of a PDE solver that is capable of handling separate terms either explicitly or implicitly. The simulations detailed in our paper utilize *irkc.f* to handle the diffusion terms explicitly and the growth/quiescence terms implicitly. Here, the explicit terms are computed with a couple of second-order Runge-Kutta-Chebyshev methods, while the implicit terms are handled by solving a large number of uncoupled systems via a modified Newton method with the use of the Jacobian of the implicit terms and an LU decomposition of an iteration matrix (Shampine 2006). While *irkc.f* also automatically adjusts the timestep according to the local truncation error, the simulations performed also specified a maximum timestep to ensure the simulation remains accurate over long periods of time. A more detailed explanation of *irkc.f* and its implementation is provided in Appendix II.

We first analyse the simulation’s sensitivity to the diffusion, growth, and death rates on a case-by-case basis. For all patients, an initial simulation is performed with the parameter values given in Table 1. Furthermore, for the isotropic diffusion code, the initial diffusion parameter value is set to $D = 0.04$, while the anisotropic diffusion code uses an initial

parameter value of $D = 4.0$. Given that the diffusion tensor values used by the anisotropic diffusion code are noticeably lower than 1 (with maximum values around 0.004), a given parameter value for D would result in much slower diffusion in the anisotropic case when compared to the isotropic simulations. Hence, the anisotropic case requires a larger value of D to compensate. The initial run is followed by a sequence of “experimental” runs, in which parameters are varied one at a time. The difference between the initial run and the experimental runs are used to determine the rate of change with respect to each of the five parameters. The sensitivity of the simulation to these parameters can be inferred from the maximum rate of change. A high rate of change for a parameter suggests that perturbations in the parameter result in large differences in the outcome of the simulation, which in turn suggests that alterations in the given parameter may result in a more accurate simulation.

2.2.4 Finding the Best-fit Parameters

We utilize the Matlab function *fminsearch* to alter two or three parameters at a time in order to improve the accuracy of the simulation, with initial parameters as specified above. To determine the error, the simulation is run for a period of time equal to the number of days between the beginning MRI scans and the next available set of MRIs. Each voxel may be classified as belonging to the edema, the enhancing rim, or the tumor core at the end of the simulation, depending on the end time tumor cell population. These voxels are then compared with a segmentation corresponding to the end date T1 and T2 MRI scans of the patient in order to determine what percentage of the simulation accurately classifies the tumor voxels, with the Jaccard index representing the error. If $S \cap R$ represents the number of tumor voxels that are classified the same between the simulation and the patient’s actual tumor, and $S \cup R$ represents the total number of voxels that are classified as tumor voxels (either by the simulation or the MRI segmentations), the Jaccard index is computed as

$$J = 1 - \frac{S \cap R}{S \cup R}, \quad (13)$$

with a low J value indicating a high amount of overlap between simulation and segmentation voxel classifications. Thus, *fminsearch* aims to decrease J in order to increase the accuracy of the simulation.

Including the edema in the error calculations may lead to inaccurate results with regard to approximating the tumor size or shape. Generally, steroids are prescribed to patients experiencing moderate to severe edema-related symptoms, or patients who are undergoing antitumor therapy that may increase edema (Petrelli 2020). Furthermore, the model isn't fully capable of simulating edema dynamics, and does not explicitly model the dynamics of cerebral spinal fluid. As such, an accurate approximating of the edema may not be possible. Thus, a version of the error evaluation which relies only on the tumor core and enhancing rim segmentations is used to find a second set of best-fit parameters that does not consider edema. In some patients, such as 028, the second comparison set of MRIs does not contain enough tumor core or enhancing rim to estimate the best-fit parameters without considering the edema, thus the results are omitted from the results section.

Furthermore, the *fminsearch* code has only been allowed to run simulations for 48 CPU hours to find the best parameters. As a result, the code is more likely to produce accurate parameters for patients with fewer days between simulations, where *fminsearch* would be able to complete its parameter evaluation before the 48 hour CPU deadline. Conversely, patients with much longer time intervals between MRIs are, to some degree, less easily approximated with *fminsearch*. Many patients may still be accurately approximated for time intervals up to around 150 days, but *fminsearch* will require a more generous time limit for patients with time intervals of over 200 days. However, increasing the number of CPU hours *fminsearch* is allowed to search for parameters may limit the practicality of estimating patient parameters numerically. While an overly generous CPU time limit may not be a relevant concern for a post-mortem analysis, a more analytical approach (or more frequent MRIs) may be necessary for a living patient.

These best-fit parameters are then used to analyse the long-term growth of the simulated tumor over a period of several months, although the simulations may not run over several months all at once. Analysis is done by starting a simulation with initial conditions corresponding to the first set of usable MRI scans, then simulating tumor growth over a period of 100 days. The end results are then saved as a set of segmentations, which are then used to set the initial conditions for the next 100 day simulation. The choice of 100 days per simulation is arbitrary, and any time interval that does not allow the computational error to grow up to unacceptable levels can be used. For each patient, the final number of days from the first set of MRIs is determined by the time interval between the starting MRIs and some set of MRIs taken several months afterwards. If such a set is available, then the long-term simulations are run up to that point. Some patients did not have a set of comparison MRIs available several months after the initial MRI scans, so these patients have long-term runs up to a time period roughly equivalent to the other patients. In our case, patients with no long-term comparison MRIs have long-term runs 250 days out from the starting MRIs.

Table 2. The maximum rate of change in the total tumor cell population $p + q$ for the isotropic simulation, with respect to ρ_1 , ρ_2 , and D , for each patient.

Patient	$\frac{\partial(p+q)}{\partial\rho_1}$	$\frac{\partial(p+q)}{\partial\rho_2}$	$\frac{\partial(p+q)}{\partial D}$
011	$2.8504 \cdot 10^6$	$2.1963 \cdot 10^6$	$6.1983 \cdot 10^5$
018	$1.0887 \cdot 10^6$	$1.7210 \cdot 10^5$	$7.6658 \cdot 10^4$
019	$6.9390 \cdot 10^5$	$4.4887 \cdot 10^5$	$1.2703 \cdot 10^4$
026	$7.2762 \cdot 10^5$	$4.4493 \cdot 10^5$	$1.4371 \cdot 10^5$
028	$5.0140 \cdot 10^5$	$5.2096 \cdot 10^5$	$1.2002 \cdot 10^5$
029	$1.6360 \cdot 10^6$	$1.3412 \cdot 10^6$	$7.3128 \cdot 10^5$
030	$1.1499 \cdot 10^5$	$3.3968 \cdot 10^4$	$9.7022 \cdot 10^3$
036	$3.8945 \cdot 10^6$	$1.8110 \cdot 10^6$	$8.5342 \cdot 10^5$
039	$1.7057 \cdot 10^6$	$1.3965 \cdot 10^5$	$6.5091 \cdot 10^4$
045	$7.5584 \cdot 10^5$	$1.5825 \cdot 10^5$	$1.0315 \cdot 10^5$

3. Results

3.1 Parameter Sensitivity Analysis

Tables 2 through 5 contain the results of the parameter sensitivity analysis for the isotropic and anisotropic simulations. While multiple simulations with differing values for each parameter were tested, the table contains only the highest rate of change in the total tumor cell population $p + q$ from the initial simulation from any of the perturbed simulations. All test simulations required that the test parameter value differed from the initial parameter value by at least .001. Variations were made in the following parameters: ρ_1 , which refers to the growth rate in the white matter and edematous regions of the brain; ρ_2 , which refers to the growth rate in the gray matter regions as well as the enhancing rim and the tumor core; k_1 , which corresponds to the rate of quiescence in the white matter, gray matter, and edematous regions of the brain; k_2 , which corresponds to the quiescent rate in the enhancing rim; k_3 , which corresponds correspond to the quiescent rate in the tumor core; and D , which determines the rate of diffusion everywhere in the brain. In general, variations in the quiescence parameters produced negligible changes in simulation outcomes compared to variations in the proliferative and diffusion parameters. These results are discussed in more detail in the next section.

Table 3. The maximum rate of change in the total tumor cell population $p + q$ for the isotropic simulation, with respect to k_1 , k_2 , and k_3 , for each patient.

Patient	$\frac{\partial(p+q)}{\partial k_1}$	$\frac{\partial(p+q)}{\partial k_2}$	$\frac{\partial(p+q)}{\partial k_3}$
011	$8.1125 \cdot 10^5$	$5.8276 \cdot 10^5$	$7.6679 \cdot 10^6$
018	$1.9190 \cdot 10^1$	$1.9787 \cdot 10^1$	$2.0310 \cdot 10^1$
019	$3.1895 \cdot 10^1$	$2.8945 \cdot 10^1$	$3.6388 \cdot 10^1$
026	$3.1618 \cdot 10^4$	$6.7815 \cdot 10^4$	$4.8656 \cdot 10^1$
028	$2.1424 \cdot 10^4$	$1.6690 \cdot 10^4$	$9.1650 \cdot 10^0$
029	$3.4390 \cdot 10^3$	$2.5073 \cdot 10^3$	$5.6807 \cdot 10^4$
030	$1.0484 \cdot 10^{-1}$	$9.8832 \cdot 10^{-6}$	$3.1626 \cdot 10^{-6}$
036	$2.1374 \cdot 10^3$	$2.5807 \cdot 10^3$	$7.0142 \cdot 10^3$
039	$4.2625 \cdot 10^0$	$2.1121 \cdot 10^{-7}$	$1.6897 \cdot 10^{-7}$
045	$2.2868 \cdot 10^2$	$2.5834 \cdot 10^2$	$2.7792 \cdot 10^2$

Table 4. The maximum rate of change in the total tumor cell population $p + q$ for the anisotropic simulation, with respect to ρ_1 , ρ_2 , and D , for each patient. Results are shown for the anisotropic diffusion simulations.

Patient	$\frac{\partial(p+q)}{\partial \rho_1}$	$\frac{\partial(p+q)}{\partial \rho_2}$	$\frac{\partial(p+q)}{\partial D}$
011	$3.0229 \cdot 10^6$	$1.3092 \cdot 10^5$	$1.3005 \cdot 10^3$
018	$6.9569 \cdot 10^5$	$6.4475 \cdot 10^4$	$2.1530 \cdot 10^2$
019	$6.3770 \cdot 10^5$	$1.1246 \cdot 10^5$	$3.1874 \cdot 10^1$
026	$1.9408 \cdot 10^5$	$1.3832 \cdot 10^5$	$4.5100 \cdot 10^2$
028	$2.0917 \cdot 10^5$	$7.6429 \cdot 10^4$	$2.9677 \cdot 10^2$
029	$1.4229 \cdot 10^5$	$3.8524 \cdot 10^4$	$4.2280 \cdot 10^2$
030	$1.7280 \cdot 10^5$	$7.9960 \cdot 10^3$	$4.7867 \cdot 10^1$
036	$3.4829 \cdot 10^6$	$2.0755 \cdot 10^5$	$1.6793 \cdot 10^3$
039	$1.6441 \cdot 10^6$	$2.6467 \cdot 10^4$	$2.8098 \cdot 10^2$
045	$8.0233 \cdot 10^6$	$1.3033 \cdot 10^7$	$6.5014 \cdot 10^5$

Table 5. The maximum rate of change in the total tumor cell population $p + q$ for the anisotropic simulation, with respect to k_1 , k_2 , and k_3 , for each patient.

Patient	$\frac{\partial(p+q)}{\partial k_1}$	$\frac{\partial(p+q)}{\partial k_2}$	$\frac{\partial(p+q)}{\partial k_3}$
011	$1.9740 \cdot 10^5$	$1.7374 \cdot 10^6$	$7.7349 \cdot 10^6$
018	$3.3791 \cdot 10^0$	$1.1194 \cdot 10^3$	$6.076 \cdot 10^{-1}$
019	$2.2337 \cdot 10^{-1}$	$7.7582 \cdot 10^{-1}$	$8.4232 \cdot 10^{-1}$
026	$2.1475 \cdot 10^4$	$5.8631 \cdot 10^5$	$6.6508 \cdot 10^0$
028	$1.4070 \cdot 10^4$	$3.5741 \cdot 10^5$	$3.2115 \cdot 10^{-1}$
029	$7.3850 \cdot 10^2$	$3.8974 \cdot 10^3$	$1.4851 \cdot 10^4$
030	$1.0093 \cdot 10^0$	$9.8832 \cdot 10^{-6}$	$3.5638 \cdot 10^{-3}$
036	$6.2077 \cdot 10^2$	$1.0498 \cdot 10^4$	$4.3991 \cdot 10^3$
039	$1.4219 \cdot 10^1$	$4.1213 \cdot 10^{-3}$	$6.5940 \cdot 10^{-3}$
045	$1.6258 \cdot 10^7$	$1.4780 \cdot 10^7$	$1.8581 \cdot 10^7$

3.2 Best Fit Parameters

3.2.1 With Edema

Tables 6 and 7 contains the best-fit parameters for each patient as determined by *fminsearch*, along with the error J for the given set of parameters, for the cases where the error evaluation included the edema. Here, J indicates what percentage of the simulated and actual tumors's voxel classifications do not match, with lower values suggesting a larger overlap between the simulated tumor's classification and the corresponding patient MRI's segmentations. J take values between 0 and 1, with 1 indicating all simulation voxels are incorrectly classified and 0 indicating all simulation voxels perfectly match the segmentations. For some patients, the MRI sets used for error analysis may not contain any scans that allow for accurate edema or enhancing rim approximations. As such, patients whose incomplete datasets prevent *fminsearch* from finding best-fit parameters are marked with an asterisk.

3.2.2 Without Edema

Tables 8 and 9 contains the best-fit parameters for each patient, along with the error J for the given set of parameters, for the cases where the error evaluation disregarded the edema. As before, J indicates what percentage of the simulated and actual tumors's voxel

Table 6. Best-fit parameters for each patient, together with the associated error, for the isotropic diffusion simulations. Error evaluations included the edema for these cases. A low value for J indicates a large overlap between the simulation results and the comparison MRI classifications. Patients marked with an asterisk indicate cases where the error evaluation did not find a set of parameters with any overlap with the segmentations.

Patient	ρ_1	ρ_2	D	J
011	0.0190	0.0239	0.0439	0.6963
018	0.0160	0.0191	0.004	0.2171
019*	0.0400	0.0200	0.040	1.0000
026	0.0010	0.0224	3.5e-04	0.6593
028	0.0014	0.0209	0.0165	0.8612
029	0.0475	0.0203	0.0030	0.8932
030	0.0620	0.0270	0.0620	0.9815
036	0.0405	0.0238	0.0200	0.9367
039	0.0360	0.0205	0.0280	0.5173
045	0.0678	0.0222	0.0552	0.5135

Table 7. Best-fit parameters for each patient, together with the associated error, for the anisotropic diffusion simulations. Error evaluations included the edema for these cases. A low value for J indicates a large overlap between the simulation results and the comparison MRI classifications. Patients marked with an asterisk indicate cases where the error evaluation did not find a set of parameters with any overlap with the segmentations.

Patient	ρ_1	ρ_2	D	J
011	0.0302	0.0146	31.80	0.5779
018	0.0360	0.0200	0.400	0.0832
019*	0.0400	0.0200	4.000	1.0000
026	0.0434	0.0010	1.150	0.5763
028	0.0400	0.0200	1.000	0.8516
029	0.0395	0.0198	2.800	0.7643
030	0.0540	0.0350	4.300	0.9976
036	0.0120	0.0220	1.200	0.8185
039	0.0500	0.0310	6.200	0.5759
045	0.1020	0.0197	24.60	0.5212

Table 8. Best-fit parameters for each patient, together with the associated error, for the isotropic diffusion simulations. Error evaluations disregarded the edema in these cases. A low value for J indicates a large overlap between the simulation results and the comparison MRI classifications. Patients marked with an asterisk indicate cases where the error evaluation did not find a set of parameters with any overlap with the segmentations.

Patient	ρ_1	ρ_2	D	J
011	0.0333	0.0126	0.0060	0.6804
018	0.0140	0.0280	0.0040	0.1327
019	0.1550	0.0193	0.1020	0.9337
026	0.0399	0.0200	0.1375	0.6373
028*	0.0400	0.0200	0.0400	1.0000
029	0.0405	0.0230	0.0200	0.9183
030*	0.0400	0.0200	0.0400	1.0000
036	0.0440	0.0310	0.0200	0.8481
039	0.2800	0.0140	0.0280	0.9082
045*	0.0400	0.0200	0.0400	1.0000

classifications do not match, with lower values suggesting a larger overlap between the simulated tumor’s classification and the corresponding patient MRI’s segmentations. The indices take values between 0 and 1, with 1 indicating all simulation voxels are incorrectly classified and 0 indicating all simulation voxels perfectly match the segmentations. For some patients, the MRI sets used for error analysis may not contain any scans that allow for accurate edema or enhancing rim approximations, and for other patients, the comparison MRIs may include a resection that has removed nearly all of the visible tumor, such that there are very few high-density tumor voxels available for error analysis. As such, patients whose datasets prevent *fminsearch* from finding best-fit parameters are marked with an asterisk.

3.3 Visual Results

Figures 1 through 9 contain visualizations of the simulations, along with the corresponding MRI comparisons, for the cases in which the error calculations included the edema. Similarly, Figures 10 through 14 contain visualizations of the simulations, along with the corresponding MRI comparisons, for the cases in which the error calculations disregard

Table 9. Best-fit parameters for each patient, together with the associated error, for the anisotropic diffusion simulations. Error evaluations disregarded the edema in these cases. A low value for J indicates a large overlap between the simulation results and the comparison MRI classifications. Patients marked with an asterisk indicate cases where the error evaluation did not find a set of parameters with any overlap with the segmentations.

Patient	ρ_1	ρ_2	D	J
011	0.0335	0.0111	24.60	0.6730
018	0.0420	0.0190	1.200	0.0476
019	0.1550	0.0200	16.60	0.9572
026	0.0360	0.0200	0.400	0.6370
028*	0.0400	0.0200	4.000	1.0000
029	0.0280	0.0240	2.800	0.6250
030*	0.0400	0.0200	4.000	1.0000
036	0.0120	0.0350	1.200	0.7015
039	0.2000	0.0100	3.700	0.7582
045	0.0010	0.2430	0.900	0.6561

the edema. Each figure contains four images: two images for the comparison MRIs, and two images for the best-fit simulations. The first image contains the starting T2 MRI on the left with the associated segmentations on the right, with the second image containing the enddate T2 MRI on the left and associated segmentations on the right. The third image contains the results of the best-fit isotropic simulation, with a heatmap on the left and the associated segmentations on the right. Similarly, the fourth image contains the results of the best-fit anisotropic simulation, with a heatmap on the left and the associated segmentations on the right. When viewing the heatmaps, blue represents areas of low density, while orange represents areas of high density. When viewing the segmentations, blue represents the edema, orange represents the enhancing rim, maroon represents the tumor core, and black represents areas where no growth can occur (i.e. the area is classified as a resection or CSF).

3.4 Long-term Analysis

Figure 15 through Figure 20 contain visualizations of the long-term simulations for each patient.

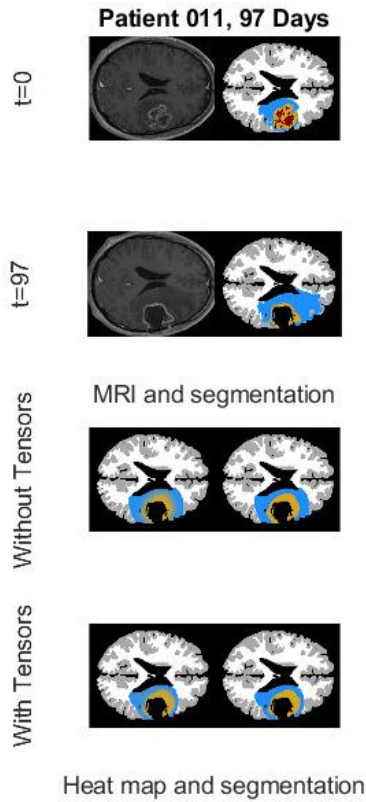


Figure 1. Most accurate simulations for patient 011, with error calculations including the edema. The starting MRI and classifications are found in the first set of images, while the end MRI and classifications are found in the second set of images. The third and fourth images contain a heatmap of the tumor cell populations (left) and the corresponding voxel classifications (right) for the isotropic and anisotropic simulations, respectively. Error calculations are performed as specified in Equation 13, where the simulation with the lowest value for J is the simulation with the largest overlap between MRI segmentations and simulated tumor classifications.

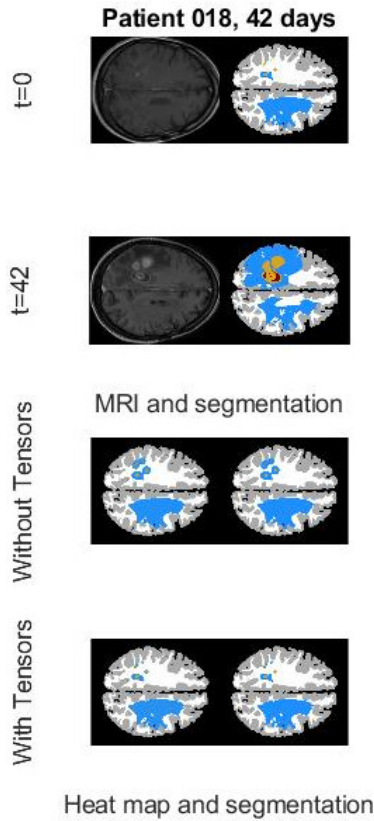


Figure 2. Most accurate simulations for patient 018, with error calculations including the edema. The starting MRI and classifications are found in the first set of images, while the end MRI and classifications are found in the second set of images. The third and fourth images contain a heatmap of the tumor cell populations (left) and the corresponding voxel classifications (right) for the isotropic and anisotropic simulations, respectively. Error calculations are performed as specified in Equation 13, where the simulation with the lowest value for J is the simulation with the largest overlap between MRI segmentations and simulated tumor classifications.

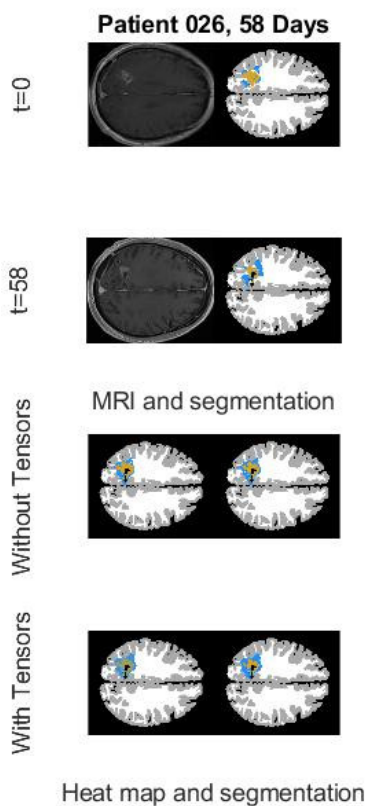


Figure 3. Most accurate simulations for patient 026, with error calculations including the edema. The starting MRI and classifications are found in the first set of images, while the end MRI and classifications are found in the second set of images. The third and fourth images contain a heatmap of the tumor cell populations (left) and the corresponding voxel classifications (right) for the isotropic and anisotropic simulations, respectively. Error calculations are performed as specified in Equation 13, where the simulation with the lowest value for J is the simulation with the largest overlap between MRI segmentations and simulated tumor classifications.

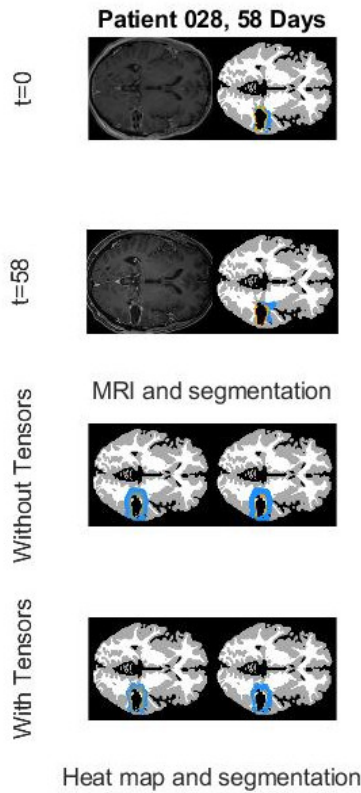


Figure 4. Most accurate simulations for patient 028, with error calculations including the edema. The starting MRI and classifications are found in the first set of images, while the end MRI and classifications are found in the second set of images. The third and fourth images contain a heatmap of the tumor cell populations (left) and the corresponding voxel classifications (right) for the isotropic and anisotropic simulations, respectively. Error calculations are performed as specified in Equation 13, where the simulation with the lowest value for J is the simulation with the largest overlap between MRI segmentations and simulated tumor classifications.

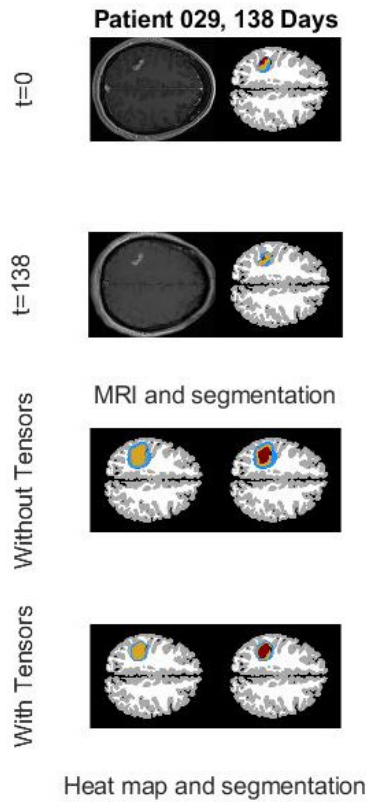


Figure 5. Most accurate simulations for patient 029, with error calculations including the edema. The starting MRI and classifications are found in the first set of images, while the end MRI and classifications are found in the second set of images. The third and fourth images contain a heatmap of the tumor cell populations (left) and the corresponding voxel classifications (right) for the isotropic and anisotropic simulations, respectively. Error calculations are performed as specified in Equation 13, where the simulation with the lowest value for J is the simulation with the largest overlap between MRI segmentations and simulated tumor classifications.

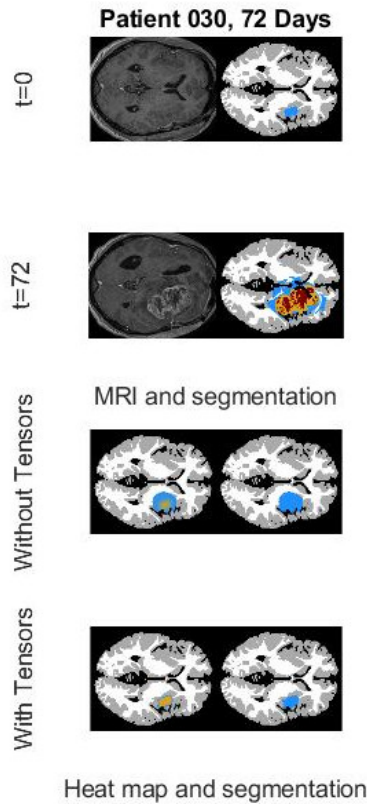


Figure 6. Most accurate simulations for patient 030, with error calculations including the edema. The starting MRI and classifications are found in the first set of images, while the end MRI and classifications are found in the second set of images. The third and fourth images contain a heatmap of the tumor cell populations (left) and the corresponding voxel classifications (right) for the isotropic and anisotropic simulations, respectively. Error calculations are performed as specified in Equation 13, where the simulation with the lowest value for J is the simulation with the largest overlap between MRI segmentations and simulated tumor classifications.

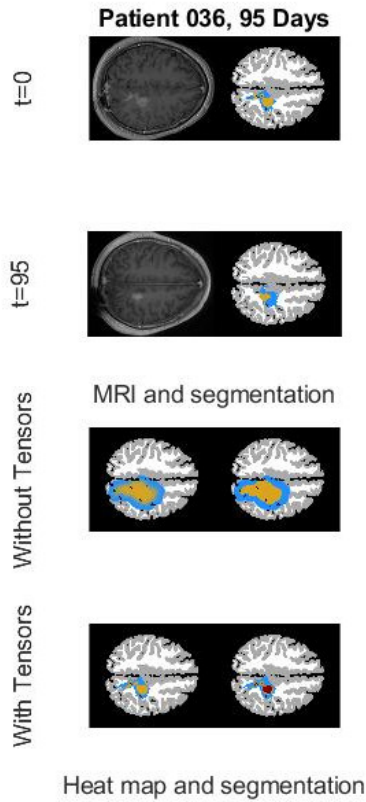


Figure 7. Most accurate simulations for patient 036, with error calculations including the edema. The starting MRI and classifications are found in the first set of images, while the end MRI and classifications are found in the second set of images. The third and fourth images contain a heatmap of the tumor cell populations (left) and the corresponding voxel classifications (right) for the isotropic and anisotropic simulations, respectively. Error calculations are performed as specified in Equation 13, where the simulation with the lowest value for J is the simulation with the largest overlap between MRI segmentations and simulated tumor classifications.

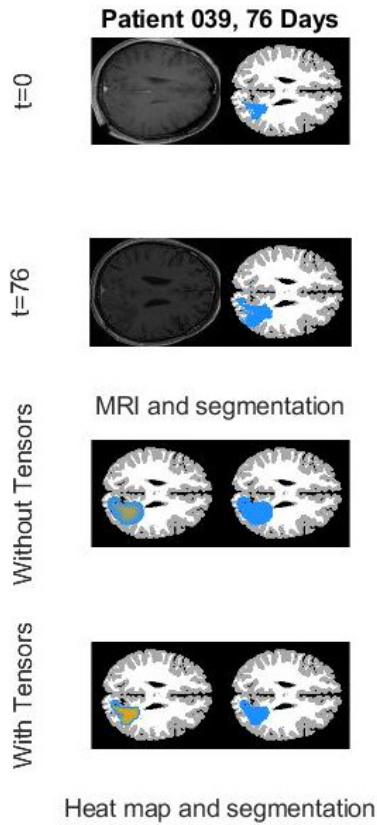


Figure 8. Most accurate simulations for patient 039, with error calculations including the edema. The starting MRI and classifications are found in the first set of images, while the end MRI and classifications are found in the second set of images. The third and fourth images contain a heatmap of the tumor cell populations (left) and the corresponding voxel classifications (right) for the isotropic and anisotropic simulations, respectively. Error calculations are performed as specified in Equation 13, where the simulation with the lowest value for J is the simulation with the largest overlap between MRI segmentations and simulated tumor classifications.

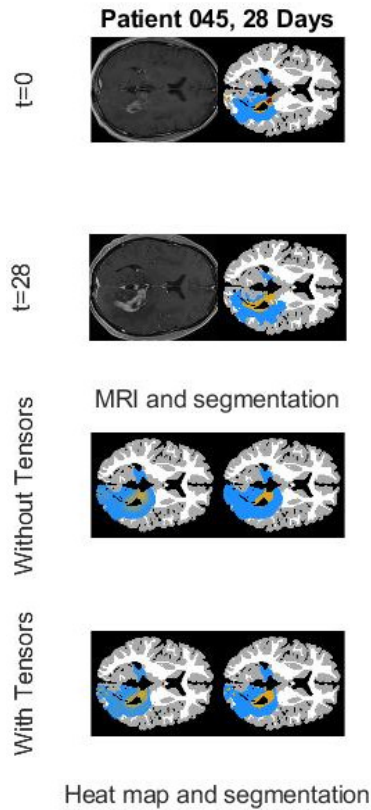


Figure 9. Most accurate simulations for patient 045, with error calculations including the edema. The starting MRI and classifications are found in the first set of images, while the end MRI and classifications are found in the second set of images. The third and fourth images contain a heatmap of the tumor cell populations (left) and the corresponding voxel classifications (right) for the isotropic and anisotropic simulations, respectively. Error calculations are performed as specified in Equation 13, where the simulation with the lowest value for J is the simulation with the largest overlap between MRI segmentations and simulated tumor classifications.

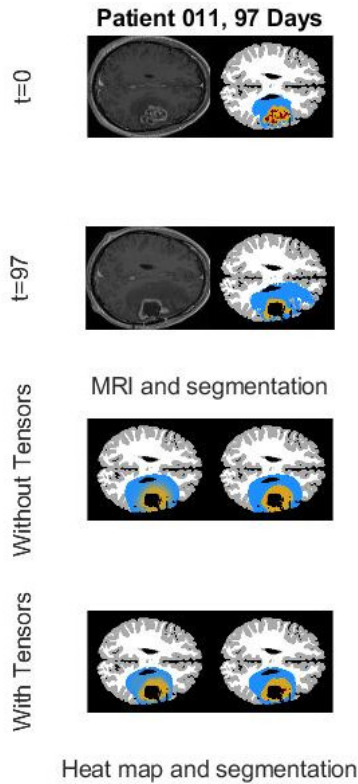


Figure 10. Most accurate simulations for patient 011, with error calculations disregarding the edema. The starting MRI and classifications are found in the first set of images, while the end MRI and classifications are found in the second set of images. The third and fourth images contain a heatmap of the tumor cell populations (left) and the corresponding voxel classifications (right) for the isotropic and anisotropic simulations, respectively. Error calculations are performed as specified in Equation 13, where the simulation with the lowest value for J is the simulation with the largest overlap between MRI segmentations and simulated tumor classifications.

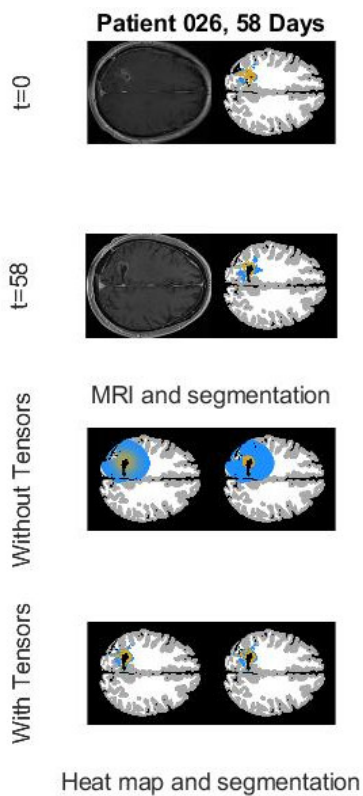


Figure 11. Most accurate simulations for patient 026, with error calculations disregarding the edema. The starting MRI and classifications are found in the first set of images, while the end MRI and classifications are found in the second set of images. The third and fourth images contain a heatmap of the tumor cell populations (left) and the corresponding voxel classifications (right) for the isotropic and anisotropic simulations, respectively. Error calculations are performed as specified in Equation 13, where the simulation with the lowest value for J is the simulation with the largest overlap between MRI segmentations and simulated tumor classifications.

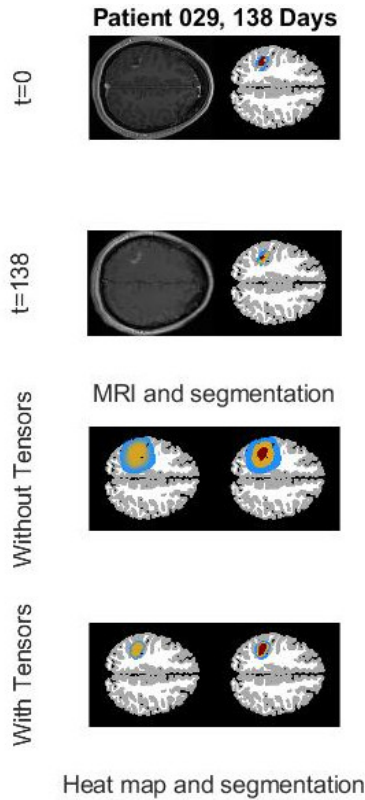


Figure 12. Most accurate simulations for patient 029, with error calculations disregarding the edema. The starting MRI and classifications are found in the first set of images, while the end MRI and classifications are found in the second set of images. The third and fourth images contain a heatmap of the tumor cell populations (left) and the corresponding voxel classifications (right) for the isotropic and anisotropic simulations, respectively. Error calculations are performed as specified in Equation 13, where the simulation with the lowest value for J is the simulation with the largest overlap between MRI segmentations and simulated tumor classifications.

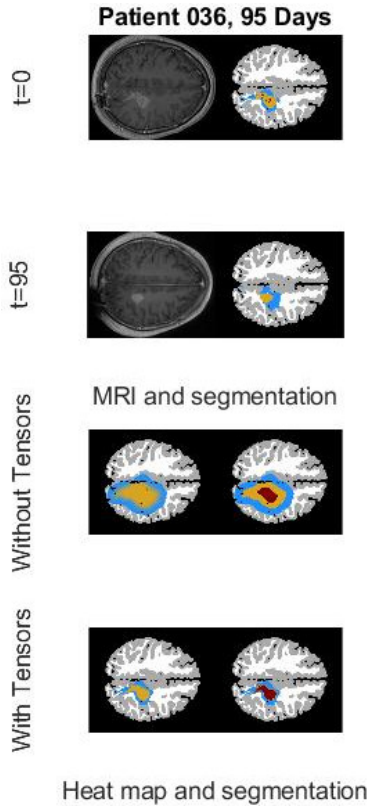


Figure 13. Most accurate simulations for patient 036, with error calculations disregarding the edema. The starting MRI and classifications are found in the first set of images, while the end MRI and classifications are found in the second set of images. The third and fourth images contain a heatmap of the tumor cell populations (left) and the corresponding voxel classifications (right) for the isotropic and anisotropic simulations, respectively. Error calculations are performed as specified in Equation 13, where the simulation with the lowest value for J is the simulation with the largest overlap between MRI segmentations and simulated tumor classifications.

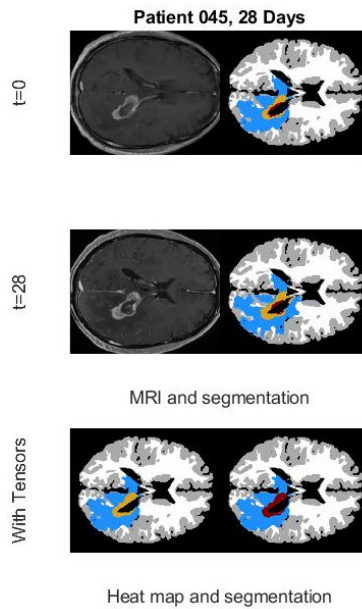


Figure 14. Most accurate simulations for patient 045, with error calculations disregarding the edema. The starting MRI and classifications are found in the first set of images, while the end MRI and classifications are found in the second set of images. The third images contain a heatmap of the tumor cell populations (left) and the corresponding voxel classifications (right) for the anisotropic simulations only. Error calculations are performed as specified in Equation 13, where the simulation with the lowest value for J is the simulation with the largest overlap between MRI segmentations and simulated tumor classifications.

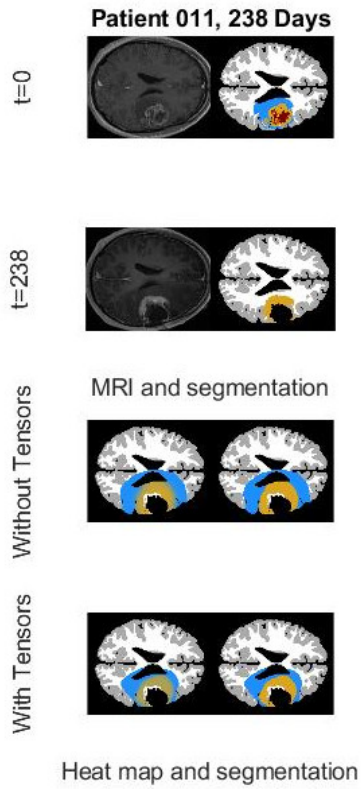


Figure 15. Long-term growth over 238 days for patient 011, as determined by the best-fit parameters. Results are compared with the relevant MRI scan.

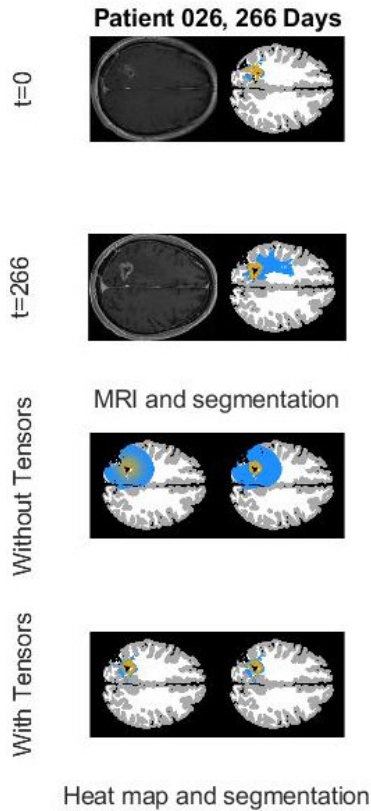


Figure 16. Long-term simulation over 266 days for patient 026, as determined by the best-fit parameters. Results are compared with the relevant MRI scan.

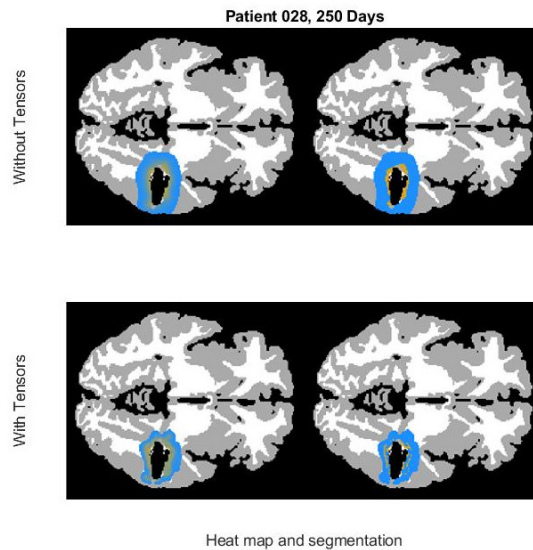


Figure 17. Long-term simulation over 250 days for patient 028, as determined by the best-fit parameters. No set of patient MRIs is available 250 days after the initial MRIs.

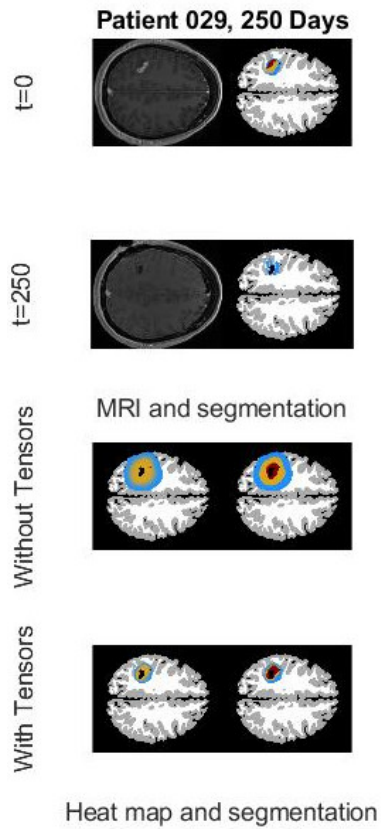


Figure 18. Long-term simulation over 250 days for patient 029, as determined by the best-fit parameters. Results are compared with the relevant MRI scan.

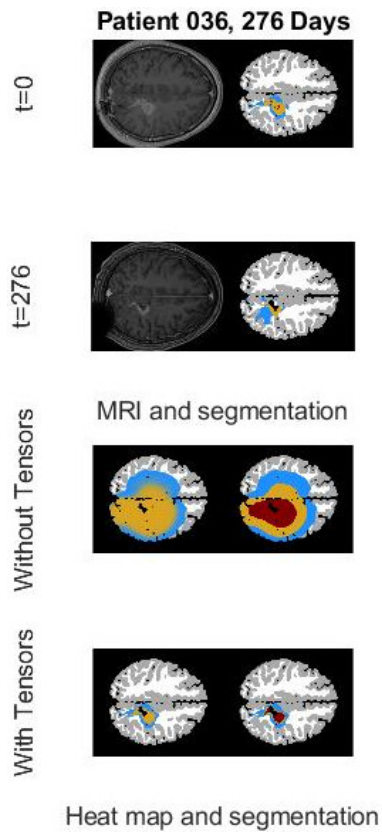


Figure 19. Long-term simulation over 276 days for patient 036, as determined by the best-fit parameters. Results are compared with the relevant MRI scan.

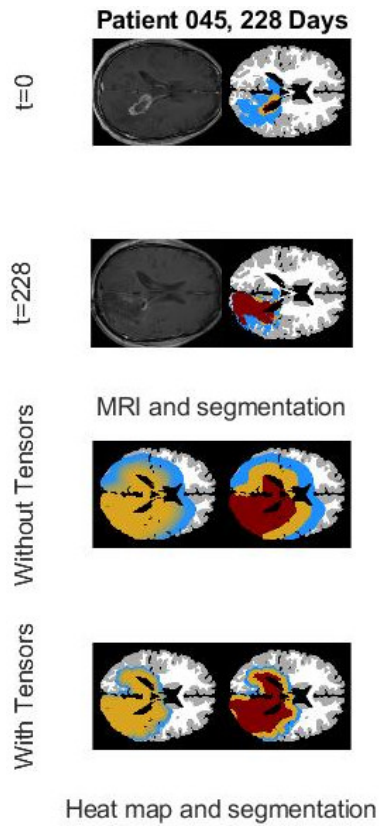


Figure 20. Long-term simulation over 228 days for patient 045, as determined by the best-fit parameters. Results are compared with the relevant MRI scan.

4. Discussion

The results of the parameter sensitivity analysis suggest that, in all cases, each patient's simulation is susceptible to changes in the proliferative and diffusion parameters, with the quiescence parameters having very little impact on the outcome of the simulations, with only a couple of simulations displaying any change in outcomes as a result of perturbations in the quiescence parameters. However, even the simulations with the greatest response to these perturbations, such as 011 and 045, experienced a negligible increase in accuracy after running *fminsearch* on these parameters. Given the low impact of these parameters on the outcome of the simulations, the best-fit quiescence parameters have been left out of Table 6 and Table 7, and have been left at the default values of $k_1 = 0.01$, $k_2 = 0.02$, and $k_3 = 0.04$ in all cases. While the table suggests that changes in D have less impact for the anisotropic code as opposed to the isotropic code, the perturbations in D were larger in relation to the default value for the isotropic code ($D = 0.04$) when compared to the default value for the anisotropic code ($D = 4.0$). In practice, larger perturbations in D were necessary for the anisotropic code to compute accurate simulations of tumor growth.

In terms of the best-fit parameters, we refer to Figures 21 and 22 for a visualization of the results. We find that, for both the isotropic diffusion and anisotropic diffusion simulations, patients 011 and 045 have a noticeably higher diffusion coefficient than the other patients. Additionally, while Figure 22 suggests that 036 has a relatively large diffusion coefficient compared to the other cases, the visual results displayed in Figure 7 suggest patient 036's best-fit parameters do not provide an accurate estimate, and a diffusion coefficient closer to patients 026, 028, and 029 may be more appropriate. Given the accuracy of patients 011 and 045, it appears the simulations most accurately approximate patients with highly diffusive tumors. Conversely, anisotropic diffusion simulations with low diffusion parameter values and high ρ_2 values were not accurate approximations, while isotropic diffusion simulations with low diffusion parameter and relatively high ρ_1 values were also not accurate

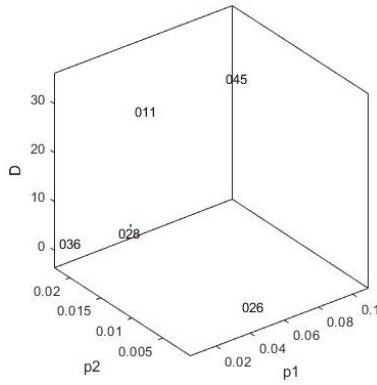


Figure 21. Plot of the best-fit parameters for six patients, for the anisotropic diffusion simulations

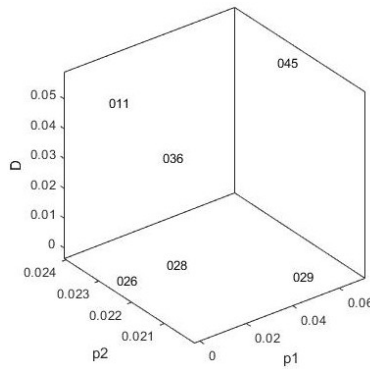


Figure 22. Plot of the best-fit parameters for six patients, for the isotropic diffusion simulations

approximations. In both cases, 026 is the standout case. With its low to average parameters values across the board, both sets of simulations should not be accurate approximations. However, both sets of simulations produced results on par with patient 011 in terms of accuracy, suggesting that the other low-diffusion patients with inaccurate results may simply need lower ρ_1 and/or ρ_2 values.

Furthermore, the anisotropic diffusion simulations take noticeably less time than the isotropic diffusion simulations. As an example, we take patient 036, whose maximum stepsizes and time intervals did not differ between simulations. While there is quite a bit of variance in computation time (which is likely tied to the overall size of the tumor/edema), the fastest isotropic diffusion simulation for 036 still took over 20,000 seconds, as opposed

to the slowest anisotropic diffusion simulation, which took just under 18,500 seconds. That said, there does not appear to be any significant drawback in terms of computational error. When comparing the best results for the isotropic diffusion and anisotropic diffusion simulations, the anisotropic diffusion simulation appears to have a maximum error of around $1.5192 \cdot 10^{-5}$, while the isotropic diffusion simulation has a maximum error of around $8.1766 \cdot 10^{-6}$. Hence, the increase in speed does not come at a significant cost with respect to computational accuracy.

In terms of the accuracy of the simulations, the anisotropic diffusion simulations nearly always produce more accurate results when compared to the isotropic diffusion simulations. While there are some patient cases where some obvious alterations may be made to the parameters of the isotropic diffusion code to produce better results, such as patients 036 and 029, *fminsearch* is constrained to a 48 CPU hour time limit per parameter. Hence, the fact that *fminsearch* can run more anisotropic diffusion simulations (due to the aforementioned increase in speed over the isotropic diffusion simulations) allows for a more accurate approximation of the patient's parameters.

5. Conclusion

In most cases, the simulations produce more accurate results via anisotropic diffusion, as opposed to isotropic diffusion. Furthermore, the patients with the least accurate simulations are those with a tumor that appears to grow very little (or even shrink) between MRIs. Conversely, the simulations accurately approximate tumors with higher rates of growth and/or diffusion, with the most accurate approximations occurring in patients with a large amount of edema.

Further analysis could consider variations in the initial conditions, such as a nonzero initial quiescent population, a gradual decrease in tumor cell populations towards the outer edge of the tumor/edema as opposed to a strict cutoff, or initial conditions based on equations found in other works, the inclusion of the mass effect of the tumor, the inclusion of various radiation treatments in the death term, the inclusion of a second type of proliferative cell to account for drug resistance, comparisons between other models with growth, death, and diffusion terms, and variations in simulation outcomes as a result of varying MRI segmentations (Murray 2003, Rockne 2008).

BIBLIOGRAPHY

- “3D Slicer”. www.slicer.org.
- Eikenberry, S. E., T. Sankar, M. C. Preul, E. J. Kostelich, C. J. Thalhauser, Y. Kuang. 2009. Virtual glioblastoma: growth, migration and treatment in a three-dimensional mathematical model. *Cell Proliferation* 42: 511–528.
- Fisher, R. A. 1937. The wave of advance of advantageous genes. *Annals of Eugenics* 7 : 355-369.
- Han, L., S. E. Eikenberry, C. He, L. Johnson, M. C. Preul, E. J. Kostelich, Y. Kuang. 2019. Patient-specific parameter estimates of glioblastoma multiforme growth dynamics from a model with explicit birth and death rates. *Mathematical Biosciences and Engineering* 16 : 5307-5323.
- Kikinis, R., S.D. Pieper, K. Vosburgh. 2014. 3D Slicer: a platform for subject-specific image analysis, visualization, and clinical support. *Intraoperative Imaging Image-Guided Therapy* 19: 277–289.
- Mahan, M. Y., A. P. Georgopoulos. 2013. Motor directional tuning across brain areas: directional resonance and the role of inhibition for directional accuracy. *Frontiers in Neural Circuits* 7 : 92.
- Murray, J. D. 2012. Glioblastoma brain tumors: estimating the time from brain tumor initiation and resolution of a patient survival anomaly after similar treatment protocols. *J. Biol. Dyn.*: 118-127.
- Murray, J. D. 2003. *Mathematical biology II: spatial models and biomedical applications, third edition*. New York, NY: Springer-Verlag New York, Incorporated.
- Petrelli, F., A. De Stefani, A. Ghidini, L. Bruschi, V. Riboldi, L. Dottorini, A. Iaculli, A. Zaniboni, F. Trevisan. 2020. Steroids use and survival in patients with glioblastoma multiforme: a pooled analysis. *Journal of Neurology*.
- Rockne, R., E. C. Alvord, J. K. Rockhill, K. R. Swanson. 2008. A mathematical model for brain tumor response to radiation therapy. *Journal of Mathematical Biology* 58 : 561–578.
- Rutter, E. M., T. L. Stepien, B. J. Anderies, J. D. Plasencia, E. C. Woolf, C. S. Adrienne, G. H. Turner, Q. Liu, D. Frakes, V. Kodibagkar, Y. Kuang, M. C. Preul, E. J. Kostelich. 2017. Mathematical analysis of glioma growth in a murine model. *Scientific Reports* 7 : 2508.
- Shampine, L.f., B. P. Sommeijer, J. G. Verwer. 2006. IRKC: an IMEX solver for stiff diffusion-reaction PDEs. *Journal of Computational and Applied Mathematics* 196 : 485-497.

“SPM - Statistical Parametric Mapping”. www.fil.ion.ucl.ac.uk.

Stupp, R., W. P. Mason, M. J. van den Bent, M. Weller, B. Fisher, M. J. B. Taphoorn, K. Belanger, A. A. Brandes, C. Marosi, U. Bogdahn, J. Curschmann, R. C. Janzer, S. K. Ludwin, T. Gorlia, A. Allgeier, D. Lacombe, J. G. Cairncross, E. Eisenhauer, R. O. Mirimanoff. 2005. Radiotherapy plus concomitant and adjuvant temozolomide for glioblastoma. *N Engl J Med* 352 : 987-996.

Swanson, K. R., R. C. Rostomily, E. C. Alvord. 2008. A mathematical modelling tool for predicting survival of individual patients following resection of glioblastoma: a proof of principle. *Br. J. Cancer* 98 : 113-119.

Zhang, S., Arfanakis, K. 2018. Evaluation of standardized and study-specific diffusion tensor imaging templates of the adult human brain: template characteristics, spatial normalization accuracy, and detection of small inter-group FA differences. *Neuroimage* 172 : 40-50.

APPENDIX I

FINITE DIFFERENCE IMPLEMENTATION

The rate of change with respect to the diffusive term is calculated via a finite difference method. The isotropic diffusion code performs these calculations with a 27-point stencil, computing the sum of the derivatives in the x , xy , xz , y , yz , and z directions. While the anisotropic code performs utilizes a 27-point stencil to calculate derivatives in the x , y , and z directions, not all points in the stencil contribute to these derivatives. For the following illustrations, we let i , j , and k refer to the indices of the voxel in the x , y , and z directions, respectively.

For the isotropic code, the second derivative is computed directly with a central finite difference scheme, then multiplied by the diffusion coefficient associated with the voxel. For example, if we let $D_{i,j,k}$ represent the diffusion value for voxel $u_{i,j,k}$, and we let $u_{i,j,k}^{xx}$, $u_{i,j,k}^{xy}$, $u_{i,j,k}^{xz}$, $u_{i,j,k}^{yy}$, $u_{i,j,k}^{yz}$, $u_{i,j,k}^{zz}$, and $u_{i,j,k}^{xyz}$ represent the contributions to the second derivative in the x , xy , xz , y , yz , z , and xyz directions, respectively, then the second derivative would be computed by first computing

$$\begin{aligned}
u_{i,j,k}^{xx} &= \frac{u_{i+1,j,k} - 2u_{i,j,k} + u_{i-1,j,k}}{\Delta x^2}, \\
u_{i,j,k}^{yy} &= \frac{u_{i,j+1,k} - 2u_{i,j,k} + u_{i,j-1,k}}{\Delta y^2}, \\
u_{i,j,k}^{zz} &= \frac{u_{i,j,k+1} - 2u_{i,j,k} + u_{i,j,k-1}}{\Delta z^2}, \\
u_{i,j,k}^{xy} &= \frac{u_{i-1,j+1,k} + u_{i-1,j-1,k} - 4u_{i,j,k} + u_{i+1,j+1,k} + u_{i+1,j-1,k}}{(\Delta x^2 + \Delta y^2)}, \\
u_{i,j,k}^{xz} &= \frac{u_{i-1,j,k+1} + u_{i-1,j,k-1} - 4u_{i,j,k} + u_{i+1,j,k+1} + u_{i+1,j,k-1}}{(\Delta x^2 + \Delta z^2)}, \\
u_{i,j,k}^{yz} &= \frac{u_{i,j+1,k+1} + u_{i,j+1,k-1} - 4u_{i,j,k} + u_{i,j-1,k+1} + u_{i,j-1,k-1}}{(\Delta y^2 + \Delta z^2)}, \\
u_{i,j,k}^{xyz} &= \frac{u_{i+1,j+1,k+1} + u_{i+1,j+1,k-1} - 4u_{i,j,k} + u_{i+1,j-1,k+1} + u_{i+1,j-1,k-1}}{(\Delta x^2 + \Delta y^2 + \Delta z^2)} \\
&\quad + \frac{u_{i-1,j+1,k+1} + u_{i-1,j+1,k-1} - 4u_{i,j,k} + u_{i-1,j-1,k+1} + u_{i-1,j-1,k-1}}{(\Delta x^2 + \Delta y^2 + \Delta z^2)},
\end{aligned}$$

then by computing

$$\nabla \cdot (D(x)\nabla(u_{i,j,k})) = D_{i,j,k} (u_{i,j,k}^{xx} + u_{i,j,k}^{yy} + u_{i,j,k}^{zz} + u_{i,j,k}^{xy} + u_{i,j,k}^{xz} + u_{i,j,k}^{yz} + u_{i,j,k}^{xyz})$$

For the anisotropic code, since the diffusion coefficient is replaced with a diffusion tensor, first derivatives are computed with a backward difference method in the x , y , and z directions only. These values are used to form a gradient that is then multiplied on the left by the diffusion tensor. The second derivative is then calculated from the first derivatives with a forward difference method. For example, if we let $D_{i,j,k}$ refer to the diffusion tensor for the voxel $u_{i,j,k}$, with $D_{i,j,k}^{xx}$, $D_{i,j,k}^{xy}$, $D_{i,j,k}^{xz}$, $D_{i,j,k}^{yy}$, $D_{i,j,k}^{yz}$, and $D_{i,j,k}^{zz}$ referring to the individual diffusion tensor values in the x , xy , xz , y , yz , z directions, respectively, then the first

derivative at a voxel $u_{i,j,k}$ would be computed by

$$\begin{aligned} u_{i,j,k}^{xx} &= \frac{u_{i,j,k} - u_{i-1,j,k}}{\Delta x}, \\ u_{i,j,k}^{yy} &= \frac{u_{i,j,k} - u_{i,j-1,k}}{\Delta y}, \\ u_{i,j,k}^{zz} &= \frac{u_{i,j,k} - u_{i,j,k-1}}{\Delta z}, \end{aligned}$$

which is then followed by computing

$$\begin{pmatrix} D_{i,j,k}^{xx} & D_{i,j,k}^{xy} & D_{i,j,k}^{xz} \\ D_{i,j,k}^{yx} & D_{i,j,k}^{yy} & D_{i,j,k}^{yz} \\ D_{i,j,k}^{zx} & D_{i,j,k}^{zy} & D_{i,j,k}^{zz} \end{pmatrix} \begin{pmatrix} u_{i,j,k}^x \\ u_{i,j,k}^y \\ u_{i,j,k}^z \end{pmatrix} = \begin{pmatrix} D_{i,j,k}^{xx}u_{i,j,k}^x + D_{i,j,k}^{xy}u_{i,j,k}^y + D_{i,j,k}^{xz}u_{i,j,k}^z \\ D_{i,j,k}^{yx}u_{i,j,k}^x + D_{i,j,k}^{yy}u_{i,j,k}^y + D_{i,j,k}^{yz}u_{i,j,k}^z \\ D_{i,j,k}^{zx}u_{i,j,k}^x + D_{i,j,k}^{zy}u_{i,j,k}^y + D_{i,j,k}^{zz}u_{i,j,k}^z \end{pmatrix},$$

which is abbreviated as

$$\begin{pmatrix} D_{i,j,k}u_{i,j,k}^x \\ D_{i,j,k}u_{i,j,k}^y \\ D_{i,j,k}u_{i,j,k}^z \end{pmatrix}.$$

Similar calculations for the voxels $u_{i+1,j,k}$, $u_{i,j+1,k}$, and $u_{i,j,k+1}$ are performed to calculate

$$\begin{aligned} \begin{pmatrix} D_{i+1,j,k}^{xx}u_{i+1,j,k}^x + D_{i+1,j,k}^{xy}u_{i+1,j,k}^y + D_{i+1,j,k}^{xz}u_{i+1,j,k}^z \\ D_{i+1,j,k}^{yx}u_{i+1,j,k}^x + D_{i+1,j,k}^{yy}u_{i+1,j,k}^y + D_{i+1,j,k}^{yz}u_{i+1,j,k}^z \\ D_{i+1,j,k}^{zx}u_{i+1,j,k}^x + D_{i+1,j,k}^{zy}u_{i+1,j,k}^y + D_{i+1,j,k}^{zz}u_{i+1,j,k}^z \end{pmatrix} &= \begin{pmatrix} D_{i+1,j,k}u_{i+1,j,k}^x \\ D_{i+1,j,k}u_{i+1,j,k}^y \\ D_{i+1,j,k}u_{i+1,j,k}^z \end{pmatrix}, \\ \begin{pmatrix} D_{i,j+1,k}^{xx}u_{i,j+1,k}^x + D_{i,j+1,k}^{xy}u_{i,j+1,k}^y + D_{i,j+1,k}^{xz}u_{i,j+1,k}^z \\ D_{i,j+1,k}^{yx}u_{i,j+1,k}^x + D_{i,j+1,k}^{yy}u_{i,j+1,k}^y + D_{i,j+1,k}^{yz}u_{i,j+1,k}^z \\ D_{i,j+1,k}^{zx}u_{i,j+1,k}^x + D_{i,j+1,k}^{zy}u_{i,j+1,k}^y + D_{i,j+1,k}^{zz}u_{i,j+1,k}^z \end{pmatrix} &= \begin{pmatrix} D_{i,j+1,k}u_{i,j+1,k}^x \\ D_{i,j+1,k}u_{i,j+1,k}^y \\ D_{i,j+1,k}u_{i,j+1,k}^z \end{pmatrix}, \\ \begin{pmatrix} D_{i,j,k+1}^{xx}u_{i,j,k+1}^x + D_{i,j,k+1}^{xy}u_{i,j,k+1}^y + D_{i,j,k+1}^{xz}u_{i,j,k+1}^z \\ D_{i,j,k+1}^{yx}u_{i,j,k+1}^x + D_{i,j,k+1}^{yy}u_{i,j,k+1}^y + D_{i,j,k+1}^{yz}u_{i,j,k+1}^z \\ D_{i,j,k+1}^{zx}u_{i,j,k+1}^x + D_{i,j,k+1}^{zy}u_{i,j,k+1}^y + D_{i,j,k+1}^{zz}u_{i,j,k+1}^z \end{pmatrix} &= \begin{pmatrix} D_{i,j,k+1}u_{i,j,k+1}^x \\ D_{i,j,k+1}u_{i,j,k+1}^y \\ D_{i,j,k+1}u_{i,j,k+1}^z \end{pmatrix}. \end{aligned}$$

Finally, the second derivative can be computed with

$$\begin{aligned} \nabla \cdot (D(x)\nabla(u_{i,j,k})) &= \frac{D_{i+1,j,k}u_{i+1,j,k}^x - D_{i,j,k}u_{i,j,k}^x}{\Delta x} \\ &+ \frac{D_{i,j+1,k}u_{i,j+1,k}^y - D_{i,j,k}u_{i,j,k}^y}{\Delta y} \\ &+ \frac{D_{i,j,k+1}u_{i,j,k+1}^z - D_{i,j,k}u_{i,j,k}^z}{\Delta z}. \end{aligned}$$

APPENDIX II
NUMERICAL METHOD

For both versions of the code, the IRKC method is the numerical scheme used to solve the reaction-diffusion PDEs specified by equations 3 and 4, with the use of *irkc.f*. The IRKC method can be classified as an IMEX method, where some terms in the PDE are handled explicitly while other terms are handled implicitly. In particular, the IRKC method is ideal when the implicit terms cause the PDEs to be stiff (Shampine 2006). Furthermore, the use of *irkc.f* allows calculations to be performed voxel by voxel for both the reaction and diffusion terms, which allows for parallelization of the simulations. There are a number of assumptions that must be met in order to make use of *irkc.f*. For the explicit terms, the eigenvalues of the Jacobian of the explicit terms must be close to, if not on, the negative real axis. Similarly, the implicit terms require a Jacobian that is both real and negative, and the code must be able to provide the Jacobian of the implicit terms to *irkc.f* at each stage and at each voxel. Furthermore, the implicit terms at a given voxel must not depend on any of the neighboring voxels (Shampine 2006). In order to solve equations 3 and 4, the diffusion terms are handled explicitly with the use of a family of second-order Runge-Kutta-Chebyshev methods, while the reaction terms are handled implicitly with the use of a modified Newton method (Shampine 2006).

While *irkc.f* is capable of receiving a maximum timestep as input, the method chooses a stepsize with respect to the estimated local error. If y_n represents the solution at the current timestep, the local error is associated with the second-order terms in the Taylor expansion of the solution at the next timestep y_{n+1} (Shampine 2006). If no relative and absolute error tolerances are specified, the defaults are 10^{-2} for the relative error and 10^{-3} for the absolute error (Shampine 2006). For the purposes of our code, for each voxel, the code calculates

$$\text{err}_k = \sum_{i=1}^2 \left(\frac{Est_{n+1,k}^{(i)}}{10^{-3} + 10^{-2} \max(|y_{n,k}^{(i)}|, |y_{n+1,k}^{(i)}|)} \right),$$

then, with NG representing the total number of voxels (dependent on the spacial gridsize Δx of the MRI scans and the standard brain), calculates the weighted root mean square norm of the error as

$$\|Est_{n+1}\| = \sqrt{\frac{1}{2\text{NG}} \sum_{k=1}^{\text{NG}} \text{err}_k}.$$

If $\|Est_{n+1}\| > 1$, y_{n+1} is repeated with a smaller timestep. Otherwise, y_{n+1} is accepted (Shampine 2006). In either case, the new stepsize is taken to be proportional to the current timestep Δt_n , with

$$\Delta t_{\text{new}} = \min(10, \max(0.1, fac)) \Delta t_n,$$

$$fac = 0.8 \left(\frac{\|Est_n\|^{\frac{1}{2}}}{\|Est_{n+1}\|^{\frac{1}{2}} \frac{\Delta t_n}{\Delta t_{n-1}}} \right) \frac{1}{\|Est_{n+1}\|^{\frac{1}{2}}}.$$

If the modified Newton iteration fails to converge, the new stepsize is $\Delta t_n/2$ (Shampine 2006).